The application of a gravimetric forward modelling of the lithospheric structure for an estimate of the average density of the upper asthenosphere

Wenjin Chen [a], Robert Tenzer [b], *

[a] School of Geomatics Science and Technology, Nanjing Tech University, Nanjing, China
[b] Department of Land Surveying and Geo-Informatics, Hong Kong Polytechnic University, Hong Kong

A B S T R A C T

The average density of 3300 kg m^{-3} is often attributed for the asthenosphere. In this study, we inspect this value by estimating the average value of the (upper) asthenosphere based on applying the gravimetric forward modelling of major known lithospheric density structures. The LITHO1.0 global seismic model of the lithospheric density structure is used for this purpose, while considering that the lithosphere-asthenosphere boundary (LAB) is rheological, conventionally taken at the 1300 °C isotherm, above which the mantle behaves in a rigid fashion and below which it behaves in a ductile fashion. According to our result, the average density of the upper asthenosphere is roughly 3400 kg m^{-3}. This density value closely agrees with the corresponding average value 3371 kg m^{-3} computed based on an empirical density model provided in the Preliminary Reference Earth Model (PREM), while using the LITHO1.0 LAB depth data. We also demonstrate that the sub-lithospheric mantle gravity map exhibits mainly a thermal signature. The most prominent features in this gravity map are mid-oceanic spearing ridges marked by gravity lows, while oceanic subductions in the West Pacific are characterized by the most pronounced gravity highs.

1. Introduction

Seismic data are primarily used to model the Earth's inner density structure based on a conversion of seismic velocities to mass densities [1–15]. Dziewonski and Anderson [8] used this conversion to compile the Preliminary Reference Earth Model (PREM) that provides the information about seismic velocities and density structures within the whole Earth's interior by means of spherically homogenous layers. Later, a number of global and regional seismic velocity and density models have been prepared, for instance, by Kennett and Engdahl [16], Kennett et al. [17], Montagner and Kennett [18], van der Lee and Nolet [19], Grand et al. [20], Megnin and Romanowicz [21], Grand [22], Gung and Romanowicz [23], van der Lee and Frederiksen [24], Panning and Romanowicz [25], Houser et al. [26], Kustowski et al. [27,28], Bedle and van der Lee [29], Panning et al. [30], Obrebski et al. [31,32], Porritt et al. [33], James et al. [34], Lekic and Romanowicz [35], Ritsema et al. [36], Simmons et al. [13,37–39], Trabant et al. [40], French and Romanowicz [41], or Auer et al. [42].

The seismic velocity datasets were also used to compile more detailed density models of the lithosphere. Nataf and Ricard [43] prepared the crustal model based on the analysis of seismic data and additional constraints, involving the heat flow and the chemical composition. Mooney et al. [44] compiled the global crustal model CRUST5.0 with a 5° × 5° spatial resolution. The updated model CRUST2.0 was compiled with a 2° × 2° resolution [45]. The CRUST1.0 is the most recent version, complied globally on a 1° × 1° grid [46]. It consists of the ice, seawater (upper, middle, and lower)

* Corresponding author. The Department of Land Surveying and Geo-Informatics, The Hong Kong Polytechnic University, 181 Chatham Road South, Kowloon, Hong Kong.

E-mail address: robert.tenzer@polyu.edu.hk (R. Tenzer).

sediments, and (upper, middle, and lower) crystalline crustal layers, while including also a lateral density structure of the lithospheric mantle. Globally averaged data from active seismic methods and deep drilling profiles were used to predict sediment and crustal structures where no seismic measurements were available (most parts of Africa, South America, Greenland, and large oceanic areas) by a generalization to similar geological and tectonic settings. Pasyanos et al. [47] compiled the LITHO1.0 global seismic model of the lithosphere. This model was prepared in order to fit the high-resolution (Love and Rayleigh) surface wave dispersion maps using the CRUST1.0 crust data and the LLNL-G3D upper mantle model [38] as the *a priori* information. Compared to similar 3-D density and velocity models, this model provides also the information about the lithosphere-asthenosphere boundary (LAB).

Alternative methods for a recovery of the Earth's density structure involve the gravity information. The Nettleton-Parasnis technique [48,49] is often applied to estimate the near-subsurface density structure, particularly in regions without exposed outcrops, or where outcrops occurrence do not adequately represent subsurface rock densities [50,51]. The principle of this method is to find the density value in the Bouguer (topographic) gravity correction that yields zero gravity anomalies. This method works reasonably well in local applications, but cannot be applied in global studies. The main reason is that gravity disturbances reflect not only the terrain geometry, but also the lithospheric density composition. Moreover, long-wavelength variations in the free-air gravity data reflect mainly the deep mantle structure that could not be removed by applying any type of topographic gravity correction (typically involving only a simple planar Bouguer gravity reduction). Theoretically, better methods for modelling the inner density structure are based on a gravity data inversion. Several different techniques have been developed and applied for the gravity-to-density inversion. The most commonly used is the Parker-Oldenburg technique [52,53]. We could also mention more recent studies by Bear et al. [54], Camacho et al. [55], Yang H [56], Boulanger and Chouteau [57], Silva et al. [58], Mauriello et al. [59], Sichler and Hékinian [60], Silva and Barbosa [61], Montesinos, et al. [62], van Zon and Roy-Chowdhury [63], Zon et al. [64], Schiavone and Loddo [65], Fernando et al. [66], Farquharson and Mosher [67], Sun et al. [68], Toushmalani and Saibi [69], Liu et al. [70], Bijani et al. [71], Ye et al. [72] or Tian et al. [73]. Some authors applied the combined gravity and magnetic data inversion to reconstruct geologic bodies [74,75].

Techniques for the gravity data inversion work relatively well for a recovery of near-subsurface geological features, but often require the application of a gravimetric forward modelling of known density structures in order to reveal a deeper density structure or interface. These methods facilitate solutions to Newton's integral in the spatial or spectral domains. For global applications, spectral methods are preferably used [76—82]. Spectral forward and inverse modelling techniques have been applied in global studies. Sjöberg and Bagherbandi [83] and Tenzer et al. [84] applied such methods to estimate the Moho density contrast.

As mentioned above, the LITHO1.0 model provides a relatively detailed information about the 3-D density distribution within the lithosphere. Except for some regional studies, the density information below the LAB is often provided only in terms of a density change with depth. Even more remarkably, the information in available literature about the average density of the asthenosphere is somehow obscure, while mostly referring to density values of the upper mantle between 3300 and 3400 kg m^{-3}. In this study, we inspected this aspect more carefully by trying to estimate the average density of the upper asthenosphere. For this purpose, we applied the method developed by Tenzer et al. [84]. This method utilizes a gravimetric forward modelling of major known lithospheric density structures followed by a trial-and-error technique that minimizes the gravitational signature of the LAB geometry in the gravity data. In this way, the average density of the upper asthenosphere could be identified as the value for which the spatial correlation between the LAB geometry and the gravity data corrected for the gravitational contribution of the lithospheric density heterogeneities and particularly for the gravitational signature of the LAB geometry. After estimating this average density, we also present the global gravity map, which comprises mainly the gravitational signature of the asthenosphere. Based on our knowledge about the asthenosphere, we expect that this gravity map should manifests mainly a thermal signature of upwelling mantle along mid-oceanic spreading ridges and possibly also a thermal or compositional signature of deep oceanic subductions.

In the subsequent part of the article, we first summarize the expressions for the gravimetric forward modelling used to compute the gravity corrections due to the topography, lithospheric density heterogeneities and the LAB geometry. We then apply these corrections to observed (free-air) gravity data in order to reveal the gravitational signature of the asthenosphere. We also estimated the average density of the asthenosphere. The methodology we applied for this purpose is briefly reviewed in section 3. Results are presented in section 4 and major findings discussed in section 5. The study is concluded in section 6.

2. Gravimetric forward modelling

Methods for a spherical harmonic analysis and synthesis of gravitational and lithospheric structure models were applied to remove the gravitational contributions of the topography and lithospheric density heterogeneities from the (observed) free-air gravity data in order to reveal the gravitational signature of the sub-lithospheric mantle structure. The spectral expressions applied in the gravimetric forward modelling are briefly recapitulated next.

2.1. Free-air gravity disturbance

For the external convergence domain $r \geq R$, the free-air gravity disturbance δg^{FA} at a location (r, Ω) was computed from the coefficients $T_{n,m}$ of the disturbing potential T (i.e., difference between the actual and normal gravity potentials W and U respectively; $T = W - U$) using the following expression (e.g. [85])

$$\delta g^{FA}(r, \Omega) = \frac{GM}{R^2} \sum_{n=0}^{\bar{n}} \sum_{m=-n}^{n} \left(\frac{R}{r}\right)^{n+2} (n+1) \, T_{n,m} \, Y_{n,m}(\Omega) \qquad (1)$$

where $GM = 3986005 \times 10^8$ m^3 s^{-2} is the geocentric gravitational constant, $R = 6371 \times 10^3$ m is the Earth's mean radius, $Y_{n,m}$ are the surface spherical functions of degree n and order m, and $\bar{n}$ is the upper summation index of spherical harmonics. The 3-D position in Eq. (1) and thereafter is defined in the spherical coordinate system (r, Ω); where r is the radius, and $\Omega = (\varphi, \lambda)$ is the spherical direction with the spherical latitude φ and longitude λ.

2.2. Bouguer gravity disturbance

The Bouguer gravity disturbances δg^B were obtained from the free-air gravity disturbances δg^{FA} after applying the topographic g^T, ice g^I, and bathymetric g^B gravity corrections (cf. [77])

$$\delta g^B = \delta g^{FA} - g^T - g^B - g^I \qquad (2)$$

The topographic gravity correction is defined for a uniform topographic density by the following expression

$$g^{\mathrm{T}}(r,\varOmega) = \frac{GM}{R^2} \sum_{n=0}^{\bar{n}} \sum_{m=-n}^{n} \left(\frac{R}{r}\right)^{n+2}(n+1)V_{n,m}^{\mathrm{T}}\ Y_{n,m}(\varOmega) \qquad (3)$$

The potential coefficients $V_{n,m}^{\mathrm{T}}$ in Eq. (3) read

$$V_{n,m} = \frac{3}{2n+1}\frac{\rho^{\mathrm{T}}}{\bar{\rho}^{\mathrm{Earth}}} \sum_{k=0}^{n+2}\binom{n+2}{k}\frac{(-1)^k}{k+1+i}\frac{\mathrm{H}_{n,m}^{(k+1)}}{\mathrm{R}^{k+1}} \qquad (4)$$

where $\bar{\rho}^{\mathrm{Earth}} = 5500\ \mathrm{kg\ m^{-3}}$ is the Earth's mean mass density, and ρ^{T} is the (constant) topographic density. The topographic co-efficients $\{\mathrm{H}_{n,m}^{(k+1)}:\ \ k = 0,\ 1,\ ...\ \}$ are given by

$$\mathrm{H}_n^{(k+1)}(\varOmega) = \frac{2n+1}{4\pi}\iint_{\varPhi}\mathrm{H}_U^{k+1}(\varOmega')P_n(t)\ d\varOmega' = \sum_{m=-n}^{n}\mathrm{H}_{n,m}^{(k+1)}Y_{n,m}(\varOmega) \tag{5}$$

where $\mathrm{P_n}$ are the Legendre polynomials for the argument t of cosine of the spherical angle ψ between two points $(r,\varOmega)$ and $(r',\varOmega')$; i.e., $t = \cos\psi$. The infinitesimal surface element on the unit sphere is denoted as $d\varOmega' = \cos\varphi'\ d\varphi'\ d\lambda'$, and $\varPhi$ is the full spatial angle.

The ice and bathymetric gravity corrections in Eq. (2) were computed based on applying the method developed by Tenzer et al. [77] that utilizes the information about a 3-D density distribution within a particular geological unit, such as sedimentary basins. The generic expression for a spherical harmonic synthesis reads

$$g(r,\varOmega) = \frac{GM}{R^2}\sum_{n=0}^{\bar{n}}\sum_{m=-n}^{n}\left(\frac{R}{r}\right)^{n+2}(n+1)V_{n,m}\ Y_{n,m}(\varOmega) \qquad (6)$$

The potential coefficients $V_{n,m}$ of each volumetric mass layer are defined by

$$V_{n,m} = \frac{3}{2n+1}\frac{1}{\bar{\rho}^{\mathrm{Earth}}}\sum_{i=0}^{I}\left(\mathrm{Fl}_{n,m}^{(i)} - \mathrm{Fu}_{n,m}^{(i)}\right) \qquad (7)$$

where the coefficients $\{\mathrm{Fl}_{n,m}^{(i)}, \mathrm{Fu}_{n,m}^{(i)}:\ \ i = 0,\ 1,\ ...,\ I\}$ are given by

$$
\begin{aligned}
\mathrm{Fl}_{n,m}^{(i)} &= \sum_{k=0}^{n+2}\binom{n+2}{k}\frac{(-1)^k}{k+1+i}\frac{L_{n,m}^{(k+1+i)}}{\mathrm{R}^{k+1}}\\[4pt]
\mathrm{Fu}_{n,m}^{(i)} &= \sum_{k=0}^{n+2}\binom{n+2}{k}\frac{(-1)^k}{k+1+i}\frac{U_{n,m}^{(k+1+i)}}{\mathrm{R}^{k+1}}
\end{aligned}
\qquad (8)
$$

The coefficients $\{L_{n,m}^{(k+1+i)}, U_{n,m}^{(k+1+i)}:\ \ k = 0,\ 1,\ ...\ ;\ i = 1,\ 2,\ ...,\ I\}$ in Eq. (8) describe the geometry and density contrast distribution within a particular volumetric mass layer. These co-efficients are generated from discrete data (of depth, thickness and density) using the following expressions for a spherical harmonic analysis [78].

$$
L_n^{(k+1+i)}(\varOmega) =
\begin{cases}
\dfrac{2n+1}{4\pi}\iint_{\varPhi}\left[\rho(D_U,\varOmega') - \rho^{\mathrm{ref}}\right]D_L^{k+1}(\varOmega')P_n(t)\ d\varOmega' \\[10pt]
= \displaystyle\sum_{m=-n}^{n}L_{n,m}^{(k+1)}Y_{n,m}(\varOmega) \qquad\qquad\quad i = 0 \\[14pt]
\dfrac{2n+1}{4\pi}\iint_{\varPhi}\beta(\varOmega')\ \alpha_i(\varOmega')\ D_L^{k+1+i}(\varOmega')P_n(t)\ d\varOmega' \\[10pt]
= \displaystyle\sum_{m=-n}^{n}L_{n,m}^{(k+1+i)}Y_{n,m}(\varOmega) \qquad\qquad i = 1,\ 2,\ ...,\ I
\end{cases}
\qquad (9)
$$

and

$$
U_n^{(k+1+i)}(\varOmega) =
\begin{cases}
\dfrac{2n+1}{4\pi}\iint_{\varPhi}\left[\rho(D_U,\varOmega') - \rho^{\mathrm{ref}}\right]D_U^{k+1}(\varOmega')P_n(t)\ d\varOmega' \\[10pt]
= \displaystyle\sum_{m=-n}^{n}U_{n,m}^{(k+1)}Y_{n,m}(\varOmega) \qquad\qquad\quad i = 0 \\[14pt]
\dfrac{2n+1}{4\pi}\iint_{\varPhi}\beta(\varOmega')\ \alpha_i(\varOmega')\ D_U^{k+1+i}(\varOmega')P_n(t)\ d\varOmega' \\[10pt]
= \displaystyle\sum_{m=-n}^{n}U_{n,m}^{(k+1+i)}Y_{n,m}(\varOmega) \qquad\qquad i = 1,\ 2,\ ...,\ I
\end{cases}
\qquad (10)
$$

The 3-D density contrast with respect to the reference crustal density ρ^{ref} in Eqs. (9) and (10) reads

$$\delta\rho(r,\varOmega) = \rho(r,\varOmega) - \rho^{\text{ref}} = \rho(D_U,\varOmega) - \rho^{\text{ref}} + \beta(\varOmega)\sum_{i=1}^{I}\alpha_i(\varOmega)\ (\text{R}-r)^i \quad for \quad \text{R} - D_U(\varOmega) \geq r > \text{R} - D_L(\varOmega) \tag{11}$$

where $\rho(D_U,\varOmega)$ is a (nominal) value of the lateral density at a location $\varOmega$ and a depth D_U.

2.3. Crust-stripped gravity disturbance

The crust-stripped gravity disturbances δg^C were obtained from the Bouguer gravity disturbances δg^B after applying the sediment g^S and underlying (crystalline) crust g^C gravity corrections

$$\delta g^C = \delta g^B - g^S - g^C \tag{12}$$

The sediment and crust gravity corrections were computed according to the expressions given in Eqs. (6—11). These gravity data have theoretically a maximum spatial correlation with the Moho geometry (cf. [86]).

2.4. Lithosphere-stripped gravity disturbance

The lithosphere-stripped gravity disturbances δg^L were obtained from the crust-stripped gravity disturbances δg^C after applying the lithospheric-mantle gravity correction g^{LM}, i.e.

$$\delta g^L = \delta g^C - g^{LM} \tag{13}$$

For a lateral density distribution function, the lithospheric-mantle gravity correction is defined by (cf. [87]).

$$g^{LM}(r,\varOmega) = 3\frac{GM}{\text{R}^2\bar{\rho}^{\text{Earth}}}\sum_{n=0}^{\bar{n}}\frac{n+1}{2n+1}\left(\frac{\text{R}}{r}\right)^{n+2}$$

$$\times\sum_{k=0}^{n+2}\binom{n+2}{k}\frac{(-1)^k}{\text{R}^{k+1}(k+1)}\sum_{m=-n}^{n}\left(L_{n,m}^{(k+1)} - M_{n,m}^{(k+1)}\right)Y_{n,m}(\varOmega) \tag{14}$$

where $M_{n,m}^{(k+1)}$ denote the Moho coefficients, and $L_{n,m}^{(k+1)}$ are the LAB coefficients.

The Moho coefficients $M_{n,m}^{(k+1)}$ in Eq. (14) were computed according to the following integral convolution

$$\sum_{m=-n}^{n}M_{n,m}^{(k)}Y_{n,m}(\varOmega) = \frac{2n+1}{4\pi}\iint_{\varPhi}\delta\rho^{LM}(\varOmega')M^k(\varOmega')\ \text{P}_n(t)\ d\varOmega' \tag{15}$$

where M is the Moho depth, $\delta\rho^{LM}(\varOmega') = \rho^{LM}(\varOmega') - \rho^{LM}$ is a lateral density contrast ρ^{LM} (within the lithospheric mantle) with respect to the adopted reference density ρ^{LM}.

By analogy with Eq. (15), the LAB coefficients $L_{n,m}^{(k+1)}$ in Eq. (14) were computed from

$$\sum_{m=-n}^{n}L_{n,m}^{(k)}Y_{n,m}(\varOmega) = \frac{2n+1}{4\pi}\iint_{\varPhi}\delta\rho^{UM}(\varOmega')L^k(\varOmega')\ \text{P}_n(t)\ d\varOmega' \tag{16}$$

where L is the LAB depth. It is worth mentioning that all individual lithospheric density structures, such as polar glaciers, sediments, the crust, or the sub-crustal lithosphere, are mathematically treated as (non-uniform) volumetric mass density layers, instead of using a simplistic single-layer description.

2.5. Sub-lithosphere mantle gravity disturbance

The lithosphere-stripped gravity disturbances δg^L should theoretically comprise mainly the gravitational signature of the LAB geometry. To enhance a gravitational signature of the asthenosphere, the gravitational signal of the LAB geometry has to be removed from these gravity data. This procedure is realized by applying the LAB gravity correction g^{LAB} to the lithosphere-stripped gravity disturbances δg^L. The result of this numerical step yields the sub-lithosphere mantle gravity disturbances δg^A. Hence, we write

$$\delta g^A = \delta g^L - g^{LAB} \tag{17}$$

The LAB gravity correction g^{LAB} in Eq. (17) was computed as.

$$g^{LAB}(r,\varOmega) = 3\frac{GM}{\text{R}^2\bar{\rho}^{\text{Earth}}}\sum_{n=0}^{\bar{n}}\frac{n+1}{2n+1}\left(\frac{\text{R}}{r}\right)^{n+2}$$

$$\times\sum_{k=0}^{n+2}\binom{n+2}{k}\frac{(-1)^k}{\text{R}^{k+1}(k+1)}\sum_{m=-n}^{n}\widehat{L}_{n,m}^{(k+1)}\ Y_{n,m}(\varOmega) \tag{18}$$

The coefficients $\widehat{L}_{n,m}^{(k+1)}$ in Eq. (18) are defined by

$$\sum_{m=-n}^{n}\widehat{L}_{n,m}^{(k)}Y_{n,m}(\varOmega) = \frac{2n+1}{4\pi}\Delta\rho^{L/A}\iint_{\varPhi}L^k(\varOmega')\ \text{P}_n(t)\ d\varOmega' \tag{19}$$

where L is the LAB depth, and $\Delta\rho^{L/A} = \rho^A - \rho^{LM}$ is defined as the difference between the density of the (upper) asthenosphere ρ^A and the reference density of the lithospheric mantle ρ^{LM}.

3. Methodology

The gravity corrections and the corrected gravity disturbances (as described in section 2) were computed with a spectral resolution complete to the spherical harmonic degree 2160 (corresponding to a $5' \times 5'$ spatial resolution in terms of a half-wavelength), except for the gravity corrections due to density contrasts of continental sediments, the crystalline crust and the lithospheric mantle. These three gravity corrections were computed with a limited spectral resolution only up degree 180 that corresponds to a $1° \times 1°$ spatial resolution of the LITHO1.0 model. In this way, the sediment gravity correction was computed individually for the contributions of marine and continental sediments. The former was computed with a $5' \times 5'$ spatial resolution from the total sediment thickness data for the

world's oceans and marginal seas [88], while the latter only with a $1° \times 1°$ resolution using the LITHO1.0 continental sediment data.

The free-air gravity disturbances were computed from the EIGEN-6C4 [89] gravitational coefficients corrected for the GRS80 [90] normal gravity component. The topographic and ice gravity corrections were computed using the Earth2014 [91] datasets of topography and glacial bedrock relief. The value 2670 kg m^{-3} [92] was adopted to represent a uniform topographic density. The glacial density 917 kg m^{-3} (cf. [88]) was adopted to define the ice density contrast. The ice density contrast with respect to the value 2670 kg m^{-3} was used for glacier volumes above the sea level. For the glacier volumes below the sea level, the ice density contrast was taken with respect to the reference density 2900 kg m^{-3}. The LITHO1.0 sediment data, updated for sediment layers of the Antarctic continental crust according to Baranov et al. [93], were used to compute the continental sediment gravity correction. The bathymetric gravity correction was computed using the Earth2014 bathymetric depths. A depth-dependent seawater density model was utilized in the definition of the ocean density contrast. For the reference crustal density 2900 kg m^{-3} and the surface seawater density 1027.91 kg m^{-3} (cf. [94—96]), the nominal ocean density contrast (at zero depth) equals 1872.09 kg m^{-3}. The depth-dependent seawater density model was according to Eq. (11) defined by the following parameters (up to the second-order density term): $\beta = 0.00637$ kg m^{-3}, $\alpha_1 = 0.7595$ m^{-1} and $\alpha_2 = -4.3984 \times 10^{-6}$ m^{-2} (cf. [97]).

The marine sediment thickness data [98] combined with the density model of marine sediments [99] were used to compute the marine sediment gravity correction. According to Gu et al. [100], the marine sediment density model ρ^s (in kg m^{-3}) reads

$$\rho^s(T_s, D_w) \cong 1660.0 - 5.1 \times 10^{-2}D_w + 3.7 \ T_s^{0.766} \tag{20}$$

where D_w denotes the ocean-floor depth (in m), and T_s is the sediment thickness (in m). The value 1660 kg m^{-3} in Eq. (17) represents the sediment density beneath a thin sedimentary cover (for $T_s \to 0$) closely below the sea level ($D_w \to 0$). The second constituent describes the decreasing density with the ocean-floor depth (reflecting the fact that coarse particles are transported at shorter distances from the coast). The third constituent describes the increasing density with the depth within marine sediment layers (due to the compaction and further lithification); see also Chen et al. [101]. The expression in Eq. (20) was converted into a generalized form given in Eq. (11).

The LITHO1.0 data of crystalline crust density and thickness were used to compute the crust gravity correction. The lithospheric-mantle gravity correction was computed using the LITHO1.0 Moho depth, lithospheric mantle density and LAB datasets. The lithospheric mantle density contrast was defined as the LITHO1.0 lithospheric mantle density with respect to the reference density 2900 kg m^{-3}. It is important to clarify, that the density value 3200 kg m^{-3} (or 3300—3400 kg m^{-3} based on petrological evidences; e.g. [102]) is typically attributed to the lithospheric mantle. Moreover, according to the LITHO1.0 model, the lateral density within the lithospheric mantle varies from 3010 to 3460 kg m^{-3}. Nonetheless, the stripping procedure applied in this study for estimating the average density within the upper asthenosphere requires that density variations within the whole lithosphere be taken with respect to the same reference density.

Finally, we computed the LAB gravity correction. In the absence of reliable information about a lateral density distribution within the asthenosphere this computation was realized based on the principle of minimizing a spatial correlation between the sub-lithosphere mantle gravity disturbances and the LAB geometry. Practically, this computation was done so that the LAB gravity correction (Eq. (18)) was computed for different values of the density ρ^A in Eq. (19). The value ρ^A which provided a minimum spatial correlation between the sub-lithosphere mantle gravity disturbances and the LAB geometry was then selected as the average density of the upper asthenosphere.

4. Results

All gravity computations were realized globally on a $1° \times 1°$ spherical grid of surface points. Global maps of the free-air, Bouguer, crust-stripped and lithosphere-stripped gravity disturbances are shown in Fig. 1, and their statistics are summarized in Table 1.

The application of the topographic, lake, ice and bathymetric gravity corrections to the free-air gravity disturbances (Fig. 1a) revealed mainly the isostatic signature of large orogens and the gravitational signature of the ocean-floor relief in the Bouguer gravity map (Fig. 1b). Additional modifications were attributed to stripping gravity corrections due to sediments and underlying crystalline crust. The crust-stripped gravity disturbances (Fig. 1c) revealed mainly the gravitational signature of the Moho geometry. For a more detailed interpretation of intermediate results after applying these gravity corrections, we refer readers to Tenzer et al. [77,81]. The application of the lithospheric-mantle gravity correction revealed the gravitational signature of the LAB geometry in the map of the lithosphere-stripped gravity disturbances (Fig. 1d).

The average density of the upper asthenosphere was estimated based on the principle of minimizing the spatial correlation between the sub-lithosphere mantle gravity disturbances and the LAB geometry. The results of this procedure are plotted in Fig. 2. The minimum correlation was attained when using the density value of approximately 3400 kg m^{-3}. We note that the application of a more refined density step for this estimation is irrelevant due to large uncertainties of used LITHO1.0 lithospheric density model that locally could reach or even exceed ±300 kg m^{-3}.

The value of 3400 kg m^{-3} was adopted as the average density of the upper asthenosphere and consequently used to compute the LAB gravity correction and the sub-lithosphere mantle gravity disturbances. To validate the result, we repeated the computation by using the lateral density model of the asthenosphere given in the definition of PREM for the LID and LVZ layers (cf. [8]; Table 1). The expression reads

$$\rho^A(\varOmega) = 2.691 + 0.6924 \frac{R - L(\varOmega)}{R} \tag{21}$$

where R $= 6371 \times 10^3$ m and the values of the LAB depth L were taken from LITHO1.0. The lateral density model of the upper asthenosphere is shown in Fig. 3. The density values vary from 3354 to 3382 kg m^{-3}, with the mean of 3371 kg m^{-3}. This mean value quite closely agrees with our rough estimate 3400 kg m^{-3}.

The lateral density values of the upper asthenosphere (shown in Fig. 3) were used to compute the LAB gravity correction and consequently the sub-lithosphere mantle gravity disturbances. For the lateral density model, the expression in Eq. (19) used for
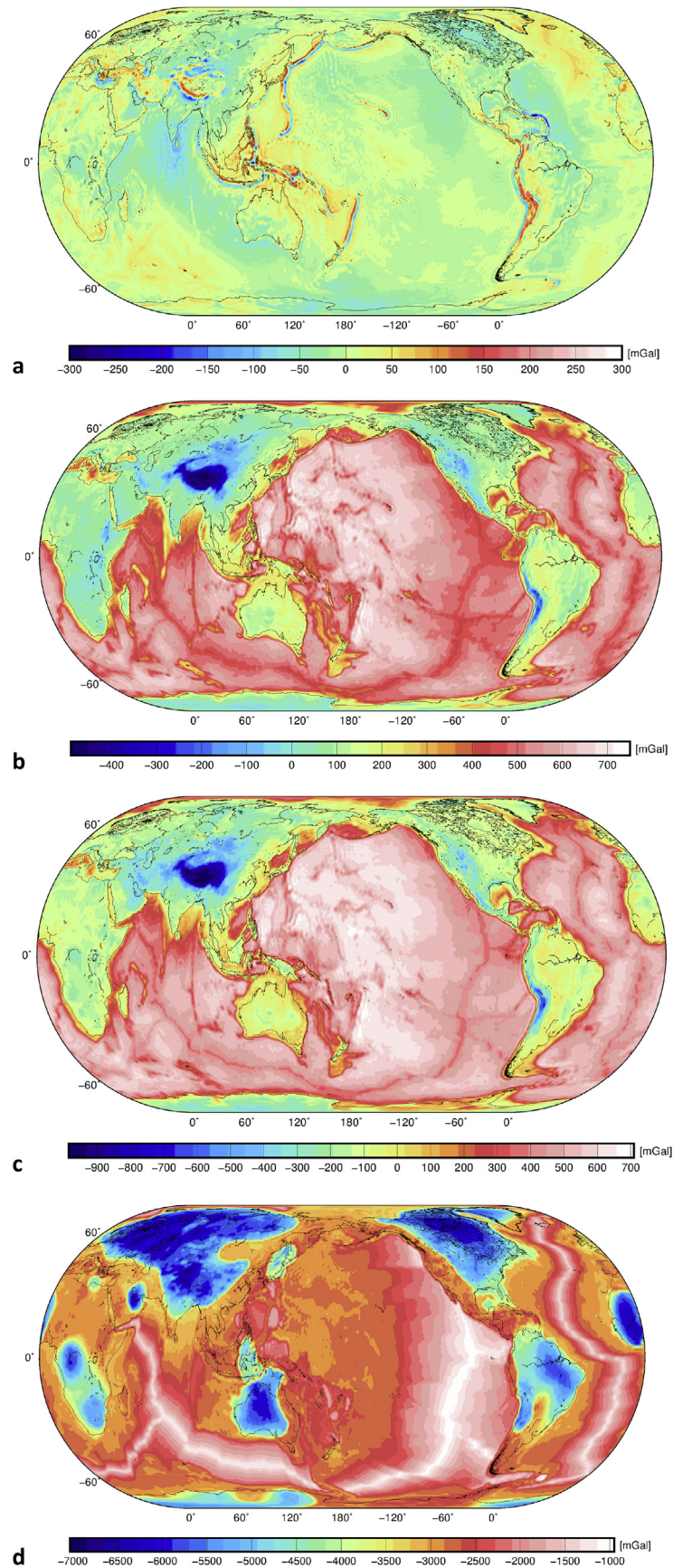
Fig. 1. Global maps of: (**a**) the free-air δg^{FA}, (**b**) Bouguer δg^{B}, (**c**) crust-stripped δg^{C}, and (**d**) lithosphere-stripped δg^{L} gravity disturbances.

Table 1
Statistics of the free-air δg^{FA}, Bouguer δg^B, crust-stripped δg^C, and lithosphere-stripped δg^L gravity disturbances.

Gravity disturbances	Min [mGal]	Max [mGal]	Mean [mGal]	STD [mGal]
δg^{FA}	−310	287	−1	30
δg^B	−492	743	329	225
δg^C	−994	712	189	316
δg^L	−7024	−949	−3216	1262

Fig. 2. Spatial correlation between the sub-lithosphere mantle gravity disturbances and the LAB geometry for different values of the average density of the upper asthenosphere.

computing the coefficients $\widehat{L}_{n,m}^{(k+1)}$ was generalized into the following form

$$\sum_{m=-n}^{n} \widehat{L}_{n,m}^{(k)}\, Y_{n,m}(\varOmega) = \frac{2n+1}{4\pi} \iint_{\Phi} \Delta\rho^{L/A}(\varOmega')L^k(\varOmega')\, P_n(t)\, d\varOmega' \tag{22}$$

where the difference $\Delta\rho^{L/A}(\varOmega) = \rho^A(\varOmega) - \rho^{LM}$ is now computed between the lateral density of the (upper) asthenosphere ρ^A and the reference density ρ^{LM}.

The results of the LAB gravity correction and the sub-lithosphere mantle gravity disturbances for the constant (average) and lateral density models of the upper asthenosphere are shown in Figs. 4 and 5 respectively; for statistics of results see Table 2.

As seen from the statistical summaries of results in Tables 1 and 2, the lithosphere-stripped gravity disturbances and the LAB gravity correction have similar spatial patterns that (more or less) closely correlate with the LAB geometry. Furthermore, both these gravity field quantities have large values of the standard deviation. Consequently, the resulting sub-lithosphere mantle gravity disturbances, obtained from the lithosphere-stripped gravity disturbances after subtracting the LAB gravity correction, are characterized by a relatively small value of the standard deviation (Table 2) due to removing the gravitational signature of the LAB geometry.

5. Discussion of results

Maps of the sub-lithosphere mantle gravity disturbances (Fig. 5) computed for the constant and lateral density models of the upper asthenosphere exhibit a very similar spatial pattern. Gravity lows detected along the mid-oceanic spreading ridges reflect a thermal signature of the upwelling mantle flow. Gravity values have an increasing trend on both size of spearing ridges that likely reflect a thermal cooling of the oceanic lithosphere and partially also the underlying upper asthenosphere. This prevailing trend of the increasing gravity with the age of the oceanic lithosphere is also clearly manifested by gravity highs over oceanic subductions in the West Pacific, and to some extent in the West Caribbean.

A surprising finding of a pronounced thermal signature under some cratons supports the hypothesis that in the thickest cratonic portions of a very fast seismic velocity (e.g. [103,104]) the cold and dense layers within the cratonic crust or the lithospheric mantle are isostatically compensated and neutrally buoyant due to the positive buoyancy of depleted cratonic mantle peridotites (cf. [105]). This signature is particularly exhibited in the gravity map computed for the PREM variable density model of the asthenosphere that is expected to be more realistic than corresponding gravity map computed for the uniform density model.
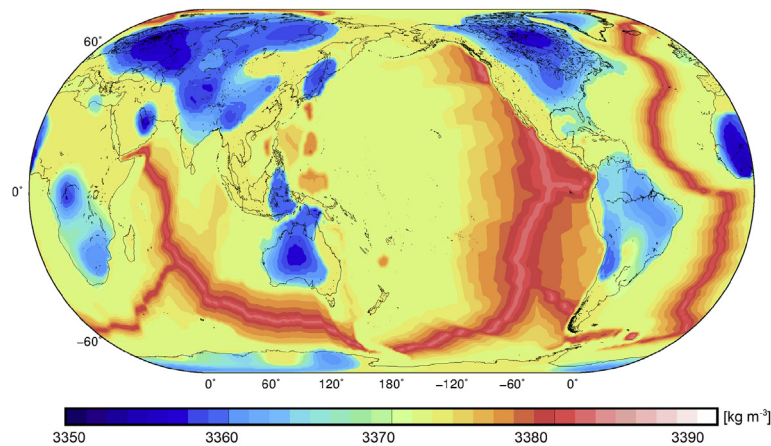

Fig. 3. The lateral density model of the upper asthenosphere according to the PREM density model and the LITHO1.0 LAB depth.
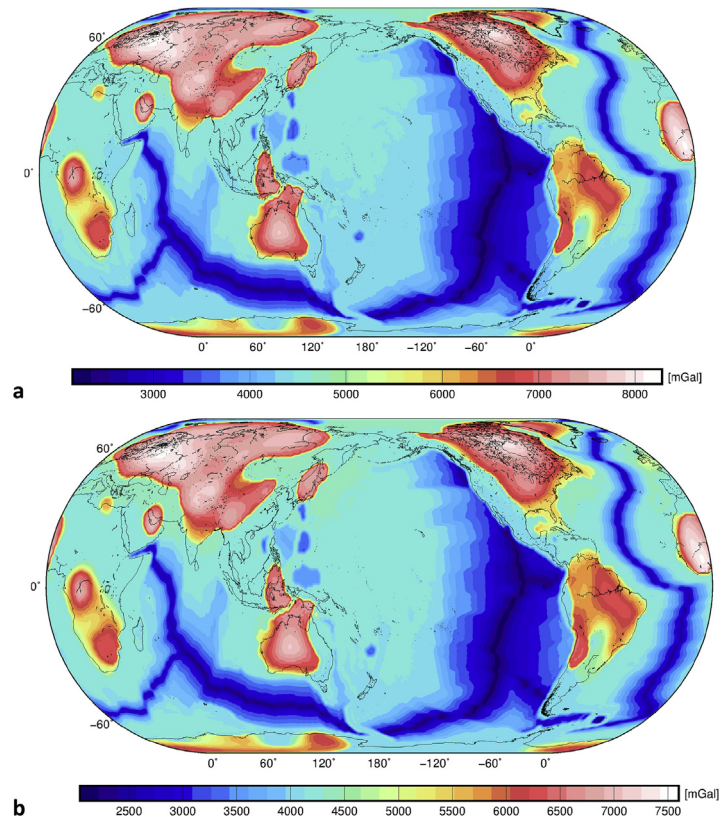
Fig. 4. Global maps of the LAB gravity correction computed for: (**a**) the constant (3400 kg m^{-3}) and (**b**) lateral (PREM) density models of the upper asthenosphere.
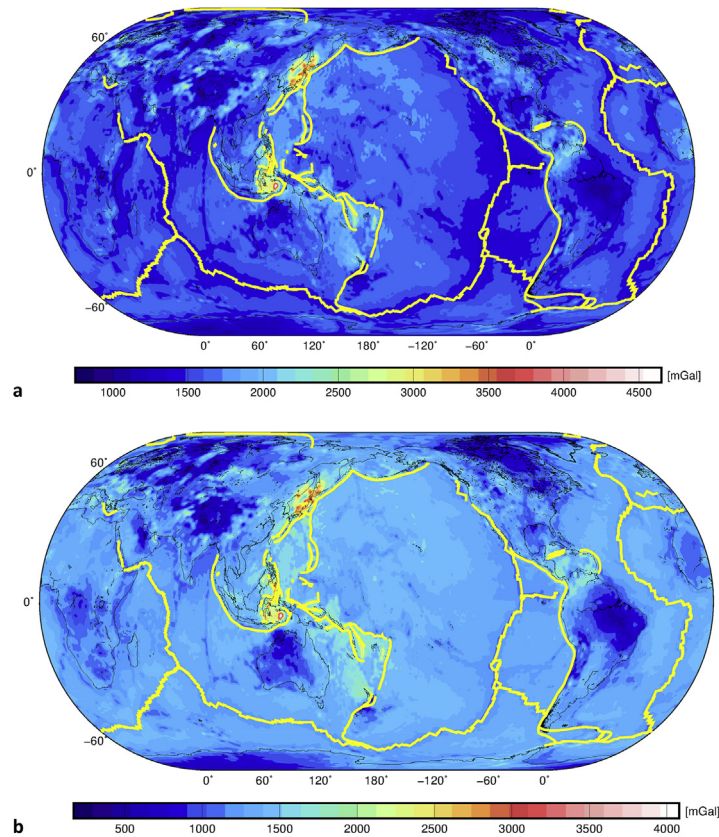

Fig. 5. Global maps of the sub-lithosphere mantle gravity disturbances computed for: (**a**) the constant (3400 kg m^{-3}) and (**b**) lateral (PREM) density models of the upper asthenosphere. Yellow lines indicate a global configuration of the mid-oceanic spreading ridges and the oceanic subduction zones.

Table 2
Statistics of the LAB gravity correction and the sub-lithosphere mantle gravity disturbances δg^A computed for the constant (3400 kg m^{-3}) and lateral (PREM) density models of the upper asthenosphere.

Gravity field quantity	Min [mGal]	Max [mGal]	Mean [mGal]	STD [mGal]
g^{LAB} for constant ρ^A	2170	8276	4764	1265
g^{LAB} for variable ρ^A	2045	7595	4462	1147
δg^A for constant ρ^A	754	4611	1548	196
δg^A for variable ρ^A	155	4083	1246	220

6. Concluding remarks

We have estimated the average density of the upper asthenosphere based on applying the gravimetric forward modelling of major known lithospheric density structures down to the LAB boundary. Our rough estimate 3400 kg m^{-3} closely agrees with the average density value 3371 kg m^{-3} computed according the PREM density equation (for the LID and LVZ layers). Both density values are larger than the mean value of 3300 kg m^{-3} typically adopted for the whole asthenosphere.

Our results of the gravimetric forward modelling also reveal that a thermal or compositional structure within the asthenosphere varies quite considerably. The sub-lithosphere mantle gravity map (compiled using either the uniform or laterally varying density models of the upper asthenosphere) exhibits a thermal state of the asthenosphere under the oceanic lithosphere, characterized by gravity lows along mid-oceanic spreading ridges and gravity highs along oceanic subductions particularly in the West Pacific. A positive buoyancy of depleted cratonic mantle peridotites could probably explain a surprising finding of a pronounced thermal signature under certain cratons.

Declarations of interest

None.

Acknowledgment

Appendix A. Supplementary data

Supplementary data to this article can be found online at https://doi.org/10.1016/j.geog.2019.04.003.

References

[1] F. Birch, The velocity of compressional waves in rocks to 10 kilobars. Part 2, J. Geophys. Res. 66 (1961) 2199–2224.
[2] F. Birch, Density and composition of mantle and core, J. Geophys. Res. 69 (20) (1964) 4377–4388.
[3] L. Knopoff, Density-velocity relations for rocks, Geophys. J. 13 (1967) 1.
[4] D.L. Anderson, A seismic equation of state, Geophys. J. R. Astron. Soc. 13 (1967) 9–30.
[5] D.L. Anderson, A universal thermal equation-of-slate, J. Geodyn. 1 (1984) 185–214.
[6] D.L. Anderson, A seismic equation of state II. Shear properties and thermodynamics of the lower mantle, Earth Planet. Sci. Lett. 45 (1987) 307–323.
[7] D.L. Anderson, J. Bass, Mineralogy and composition of the upper mantle, Geophys. Res. Lett. 11 (1984) 637–640.
[8] A.M. Dziewonski, D.L. Anderson, Preliminary reference Earth model, Phys. Earth Planet. In. 25 (4) (1981) 297–356.
[9] A.H. Lachenbruch, P. Morgan, Continental extension, magmatism and elevation; formal relations and rules of thumb, Tectonophysics 174 (1990) 39–62.
[10] S.V. Sobolev, A.Y. Babeyko, Modeling of mineralogical composition, density and elastic wave velocities in anhydrous magmatic rocks, Surv. Geophys. 15 (5) (1994) 515–544.
[11] N.I. Christensen, W.D. Mooney, Seismic velocity structure and composition of the continental crust: a global view, J. Geophys. Res. 100 (B7) (1995) 9761–9788.
[12] F. Cammarano, S. Goes, P. Vacher, D. Giardini, Inferring upper-mantle temperatures from seismic velocities, Phys. Earth Planet. In. 138 (2003) 197–222.
[13] N.A. Simmons, A.M. Forte, L. Boschi, S.P. Grand, GyPSuM: a joint tomographic model of mantle density and seismic wave speeds, J. Geophys. Res. Solid Earth 115 (2010) B12310.
[14] A. Forte, N.A. Simmons, S.P. Grand, Constraints on 3-D seismic models from global geodynamic observables: implications for the global mantle convective flow, in: G. Schubert (Ed.), Treatise of Geophysics, 805–858), second ed., Elsevier, Burlington, MA, 2015.
[15] P. Moulik, G. Ekstrom, The relationships between large-scale variations in shear velocity, density, and compressional velocity in the Earth's mantle, J. Geophys. Res.– Solid Earth 121 (2016) 2737–2771.
[16] B.L.N. Kennett, E.R. Engdahl, Travel times for global earthquake location and phase association, Geophys. J. Int. 105 (1991) 429–465.
[17] B.L.N. Kennett, E.R. Engdahl, R. Buland, Constraints on seismic velocities in the earth from travel times, Geophys. J. Int. 122 (1995) 108–124.
[18] J.P. Montagner, B.L.N. Kennett, How to reconcile body-wave and normal-mode reference Earth models? Geophys. J. Int. 125 (1995) 229–248.
[19] S. van der Lee, G. Nolet, Upper mantle S-velocity structure of North America, J. Geophys. Res. 102 (1997) 22815–22838.
[20] S.P. Grand, R.D. van der Hilst, S. Widiyantoro, Global seismic tomography: a snapshot of convection in the Earth, GSA Today (Geol. Soc. Am.) (1997) 1–7.
[21] Ch Megnin, B. Romanowicz, The shear velocity structure of the mantle from the inversion of body, surface and higher modes waveforms, Geophys. J. Int. 143 (2000) 709–728.
[22] S.P. Grand, Mantle shear-wave tomography and the fate of subducted slabs, Phil. Trans. Roy. Soc. Lond. 360 (2002) 2475–2491.
[23] Y. Gung, B. Romanowicz, Q tomography of the upper mantle using three-component long-period waveforms, Geophys. J. Int. 157 (2004) 813–830.
[24] S. van der Lee, A. Frederiksen, Surface Wave tomography applied to the North American upper mantle, in: A. Levander, G. Nolet (Eds.), AGU Monograph, Seismic Earth: Array Analysis of Broadband Seismograms, 2005, pp. 67–80.
[25] M.P. Panning, B.A. Romanowicz, A three dimensional radially anisotropic model of shear velocity in the whole mantle, Geophys. J. Int. 167 (2006) 361–379.
[26] C. Houser, G. Masters, P. Shearer, G. Laske, Shear and compressional velocity models of the mantle from cluster analysis of long-period waveforms, Geophys. J. Int. 174 (2008) 195–212.
[27] B. Kustowski, G. Ekstrm, A.M. Dziewoski, The shear-wave velocity structure in the upper mantle beneath Eurasia, Geophys. J. Int. 174 (2008a) 978–992.
[28] B. Kustowski, G. Ekstrom, A.M. Dziewonski, Anisotropic shear-wave velocity structure of the Earth's mantle: a global model, J. Geophys. Res. 113 (2008b) B06306.
[29] H. Bedle, S. van der Lee, S velocity variations beneath North America, J. Geophys. Res. 114 (2009) B07308.
[30] M.P. Panning, V. Lekic, B.A. Romanowicz, Importance of crustal corrections in the development of a new global model of radial anisotropy, J. Geophys. Res. 115 (2010) B12325.
[31] M. Obrebski, R.M. Allen, M. Xue, S.-H. Hung, Slab-plume interaction beneath the pacific Northwest, Geophys. Res. Lett. 37 (2010) L14305.
[32] M. Obrebski, R.M. Allen, F. Pollitz, S.-H. Hung, Lithosphere-asthenosphere interaction beneath the western United States from the joint inversion of body-wave travel times and surface-wave phase velocities, Geophys. J. Int. 185 (2011) 1003–1021.
[33] R.W. Porritt, R.M. Allen, D.C. Boyarko, M.R. Brudzinski, Investigation of Cascadia segmentation with ambient noise tomography, Earth Planet. Sci. Lett. 309 (1–2) (2011) 67–76.
[34] D.E. James, M.J. Fouch, R.W. Carlson, J.B. Roth, Slab fragmentation, edge flow and the origin of the Yellowstone hotspot track, Earth Planet. Sci. Lett. 311 (1) (2011) 124–135.
[35] V. Lekic, B. Romanowicz, Inferring upper-mantle structure by full waveform tomography with the spectral element method, Geophys. J. Int. 185 (2) (2011) 799–831.
[36] J. Ritsema, H.J. van Heijst, A. Deuss, J.H. Woodhouse, S40RTS: a degree-40 shear velocity model for the mantle from new Rayleigh wave dispersion, teleseismic traveltimes, and normal-mode splitting function measurements, Geophys. J. Int. 184 (2011) 1223–1236.
[37] N.A. Simmons, A.M. Forte, S.P. Grand, Thermochemical structure and dynamics of the African superplume, Geophys. Res. Lett. 34 (2007) L02301.
[38] N.A. Simmons, S.C. Myers, G. Johannesson, E. Matzel, LLNL-G3Dv3: global P wave tomography model for improved regional and teleseismic travel time prediction, J. Geophys. Res. 117 (2012) B10302.
[39] N.A. Simmons, S.C. Myers, G. Johannesson, E. Matzel, S.P. Grand, Evidence for long-lived subduction of an ancient tectonic plate beneath the southern Indian Ocean, Geophys. Res. Lett. 42 (2015) 9270–9278.

[40] C. Trabant, A.R. Hutko, M. Bahavar, R. Karstens, T. Ahern, R. Aster, Data products at the IRIS DMC: stepping-stones for research and other application, Seismic Res. Lett. 83 (6) (2012) 846–854.

[41] S.W. French, B. Romanowicz, Whole-mantle radially anisotropic shear velocity structure from spectral-element waveform tomography, Geophys. J. Int. 199 (2014) 1303–1327.

[42] L. Auer, L. Boschi, T.W. Becker, T. Nissen-Meyer, D. Giardini, Savani: a variable resolution whole-mantle model of anisotropic shear-velocity variations based on multiple datasets, J. Geophys. Res. 119 (2014) 3006–3034.

[43] H.C. Nataf, Y. Ricard, 3SMAC: an a priori tomographic model of the upper mantle based on geophysical modeling, Phys. Earth Planet. In. 95 (1996) 101–122.

[44] W.D. Mooney, G. Laske, T.G. Masters, CRUST 5.1: a global crustal model at 5° x 5°, J. Geophys. Res. 103B (1998) 727–747.

[45] C. Bassin, G. Laske, G. Masters, The current limits of resolution for surface wave tomography in North America, EOS, Trans. Am. Geophys. Union 81 (48) (2000). Fall Meeting Suppl, Abstract S12A-03.

[46] G. Laske, G. Masters, Z. Ma, M.E. Pasyanos, Update on CRUST1.0 - a 1-degree global model of Earth's crust, Geophys. Res. Abstr. 15 (2013) 2658.

[47] M.E. Pasyanos, T.G. Masters, G. Laske, Z. Ma, LITHO1.0: an updated crust and lithospheric model of the Earth, J. Geophys. Res. 119 (3) (2014) 2153–2173.

[48] L.L. Nettleton, Determination of density for reduction of gravimeter observations, Geophysics 4 (1939) 8176–8183.

[49] D.S. Parasnis, A study of rock densities in English Midlands, Geophys. J. Int. 1952 (6) (2012) 252–271.

[50] F.C. Tontini, F. Graziano, L. Cocchi, C. Carmisciano, P. Stefanelli, Determining the optimal Bouguer density for a gravity data set: implications for the isostatic setting of the Mediterranean Sea, Geophys. J. Int. 169 (2) (2007) 380–388.

[51] N. Mankhemthong, D.I. Doser, M.R. Baker, Practical estimation of near-surface bulk density variations across the border ranges fault system, central kenai peninsula, Alaska, J. Environ. Eng. Geophys. 17 (3) (2012) 51–158.

[52] R.L. Parker, The rapid calculation of potential anomalies, Geophys. J. R. Astron. Soc. 31 (1973) 447–455.

[53] D.W. Oldenburg, The inversion and interpretation of gravity anomalies, Geophysics 39 (1974) 526–536.

[54] G.W. Bear, H.J. Al-Shukri, A.J. Rudman, Linear inversion of gravity data for 3-D density distributions, Geophysics 60 (5) (1995) 1354–1364.

[55] A.G. Camacho, F.G. Montesinos, R. Vieira, A three-dimensional gravity inversion applied to São Miguel Island (Azores), J. Geophys. Res.– Solid Earth 102 (B4) (1997) 7717–7730.

[56] H. Yang, Basement density inversion using gravimetric and seismic data and the integrative interpretation, Oil Geophys. Prospect. 33 (4) (1998) 496–502.

[57] O. Boulanger, M. Chouteau, Constraints in 3D gravity inversion, Geophys. Prospect. 49 (2) (2001) 265–280.

[58] J.B.C. Silva, W.E. Medeiros, V.C.F. Barbosa, Potential-field inversion: choosing the appropriate technique to solve a geologic problem, Geophysics 66 (2) (2001) 511–520.

[59] P. Mauriello, D. Patella, Localization of maximum-depth gravity anomaly sources by a distribution of equivalent point masses, Geophysics 66 (5) (2001) 1431–1437.

[60] B. Sichler, R. Hékinian, Three-dimensional inversion of marine magnetic anomalies on the equatorial Atlantic Ridge (St. Paul Fracture Zone): delayed magnetization in a magmatically starved spreading center? J. Geophys. Res.– Solid Earth 107 (B12) (2002). EPM 7-1-EPM 7-14.

[61] J.B.C. Silva, V.C.F. Barbosa, Generalized radial inversion of 2D potential-field data, Geophysics 69 (6) (2004) 1405–1413.

[62] F.G. Montesinos, J. Arnoso, R. Vieira, Using a genetic algorithm for 3-D inversion of gravity data in Fuerteventura (Canary Islands), Int. J. Earth Sci. 94 (2) (2005) 301–316.

[63] T. van Zon, K. Roy-Chowdhury, Structural inversion of gravity data using linear programming, Geophysics 71 (3) (2006) J41–J50.

[64] T. van Zon, D. Ditmar, K.R. Chowdhury, J. Mondt, Lithotype discrimination within a gridded model by inverting gravity data, Geophys. J. Int. 170 (2) (2007) 481–491.

[65] D. Schiavone, M. Loddo, 3-D density model of Mt. Etna Volcano (Southern Italy), J. Volcanol. Geotherm. Res. 164 (3) (2007) 161–175.

[66] J.S.S.D. Fernando, C.F.B. Valéria, B.C.S. João, Adaptive Learning Gravity Inversion for 3D Salt Body Imaging, vol. 2008, SEG Technical Program Expanded Abstracts, 2008, pp. 746–750.

[67] C.G. Farquharson, C.R.W. Mosher, Three-dimensional modelling of gravity data using finite differences, J. Appl. Geophys. 68 (2009) 3.

[68] L.-P. Sun, Z. Liu, H. Shou, Y.-H. Zhang, Parameter optimization of gravity density inversion based on correlation searching and the golden section algorithm, Appl. Geophys. 9 (2) (2012) 131–138.

[69] R. Toushmalani, H. Saibi, 3D gravity inversion using tikhonov regularization, Acta Geophys. 63 (4) (2015) 1044–1065.

[70] J.-Z. Liu, L.-T. Liu, X.-H. Liang, Z.-R. Ye, 3D density inversion of gravity gradient data using the extrapolated Tikhonov regularization, Appl. Geophys. 12 (2) (2015) 137–146.

[71] R. Bijani, C.F. Ponte-Neto, D.U. Carlos, J.S.S.D. Fernando, Three-dimensional gravity inversion using graph theory to delineate the skeleton of homogeneous sources, Geophysics 80 (2) (2015) G53–G66.

[72] Z. Ye, R. Tenzer, N. Sneeuw, Comparison of methods for a 3-D density inversion from airborne gravity gradiometry, Studia Geophys. Geod. 62 (1) (2018) 1–16.

[73] Y. Tian, X. Ke, Y. Wang, DenInv3D: a geophysical software for three-dimensional density inversion of gravity field data, J. Geophys. Eng. 15 (2) (2018) 354–365.

[74] V.C.F. Barbosa, J.B.C. Silva, Reconstruction of geologic bodies in depth associated with a sedimentary basin using gravity and magnetic data, Geophys. Prospect. 59 (6) (2011) 1021–1034.

[75] L.A. Gallardo, M.A. Pérez-Flores, E. Gómez-Treviño, Refinement of three-dimensional multilayer models of basins and crustal environments by inversion of gravity and magnetic data, Tectonophysics 397 (1–2) (2005) 37–54.

[76] R. Tenzer, Hamayun, P. Vajda, Global map of the gravity anomaly corrected for complete effects of the topography, and of density contrasts of global ocean, ice, and sediments, Contrib. Geophys. Geodes. 38 (4) (2008) 357–370.

[77] R. Tenzer, Hamayun, P. Vajda, Global maps of the CRUST2.0 components stripped gravity disturbances, J. Geophys. Res. 114 (2009a) B05408.

[78] R. Tenzer, P. Novák, P. Vajda, V. Gladkikh, Hamayun, Spectral harmonic analysis and synthesis of Earth's crust gravity field, Comput. Geosci. 16 (1) (2012a) 193–207.

[79] R. Tenzer, V. Gladkikh, P. Vajda, P. Novák, Spatial and spectral analysis of refined gravity data for modelling the crust-mantle interface and mantle-lithosphere structure, Surv. Geophys. 33 (5) (2012b) 817–839.

[80] R. Tenzer, M. Bagherbandi, V. Gladkikh, Signature of the upper mantle density structure in the refined gravity data, Comput. Geosci. 16 (4) (2012d) 975–986.

[81] R. Tenzer, W. Chen, D. Tsoulis, M. Bagherbandi, L.E. Sjöberg, P. Novák, S. Jin, Analysis of the refined CRUST1.0 crustal model and its gravity field, Surv. Geophys. 36 (1) (2015a) 139–165.

[82] Z. Ye, R. Tenzer, L. Liu, Comparison of spectral and spatial methods for a Moho recovery from gravity and vertical gravity-gradient data, Studia Geophys. Geod. 61 (3) (2017) 469–496.

[83] L.E. Sjöberg, M. Bagherbandi, A method of estimating the Moho density contrast with a tentative application by EGM08 and CRUST2.0, Acta Geophys. 58 (2011) 1–24.

[84] R. Tenzer, Hamayun, P. Novák, V. Gladkikh, P. Vajda, Global crust-mantle density contrast estimated from EGM2008, DTM2008, CRUST2.0, and ICE-5G, Pure Appl. Geophys. 169 (9) (2012e) 1663–1678.

[85] W.H. Heiskanen, H. Moritz, Physical Geodesy, WH Freeman and Co, San Francisco, 1967.

[86] R. Tenzer, Hamayun, P. Vajda, A global correlation of the step-wise consolidated crust-stripped gravity field quantities with the topography, bathymetry, and the CRUST 2.0 Moho boundary, Contrib. Geophys. Geodes. 39 (2) (2009b) 133–147.

[87] R. Tenzer, W. Chen, S. Jin, Effect of the upper mantle density structure on the Moho geometry, Pure Appl. Geophys. 172 (6) (2015b) 1563–1583.

[88] J.D. Cutnell, W.J. Kenneth, Physics, third ed., Wiley, New York, 1995.

[89] Ch Förste, S.L. Bruinsma, O. Abrikosov, J.-M. Lemoine, JCh Marty, F. Flechtner, G. Balmino, F. Barthelmes, R. Biancale, in: S. Bettadpur, M. Watkins (Eds.), EIGEN-6C4 the Latest Combined Global Gravity Field Model Including GOCE Data up to Degree and Order 2190 of GFZ Potsdam and GRGS Toulouse. GFZ Data Services Tapley BD, 2014.

[90] H. Moritz, Geodetic reference system 1980, J. Geod. 74 (2000) 128162.

[91] C. Hirt, M. Rexer, Earth2014: 1 arc-min shape, topography, bedrock and ice-sheet models - available as gridded data and degree-10,800 spherical harmonics, Int. J. Appl. Earth Obs. Geoinf. 39 (2015) 103–112.

[92] W.J. Hinze, Bouguer reduction density, why 2.67? Geophysics 68 (5) (2003) 1559.

[93] A. Baranov, R. Tenzer, M. Bagherbandi, Combined gravimetric-seismic crustal model for Antarctica, Surv. Geophys. 39 (1) (2018) 23–56.

[94] V. Gladkikh, R. Tenzer, A mathematical model of the global ocean saltwater density distribution, Pure Appl. Geophys. 169 (1–2) (2011) 249–257.

[95] R. Tenzer, P. Vajda, Hamayun, A mathematical model of the bathymetry-generated external gravitational field, Contrib. Geophys. Geodes. 40 (1) (2010) 31–44.

[96] R. Tenzer, P. Novák, V. Gladkikh, On the accuracy of the bathymetry-generated gravitational field quantities for a depth-dependent seawater density distribution, Studia Geophys. Geod. 55 (4) (2011) 609–626.

[97] R. Tenzer, P. Novák, V. Gladkikh, The bathymetric stripping corrections to gravity field quantities for a depth-dependent model of the seawater density, Mar. Geodes. 35 (2012c) 198–220.

[98] D.L. Divins, Total Sediment Thickness of the World's Oceans & Marginal Seas, NOAA National Geophysical Data Center, Boulder, CO, 2003.

[99] R. Tenzer, V. Gladkikh, Assessment of density variations of marine sediments with ocean and sediment depths, Sci. World J. (2014) 9. ID 823296.

[100] X. Gu, R. Tenzer, V. Gladkikh, Empirical models of the ocean-sediment and marine sediment-bedrock density contrasts, Geosci. J. 18 (4) (2014) 439–447.

[101] W. Chen, R. Tenzer, X. Gu, Sediment stripping correction to marine gravity data, Mar. Geodes. 37 (4) (2014) 419–439.

[102] W.L. Griffin, S.Y. O'Reilly, J.C. Afonso, G.C. Begg, The composition and evolution of lithospheric mantle: a Re-evaluation and its tectonic implications, J. Petrol. 50 (7) (2009) 1185–1204.

[103] T.H. Jordan, The continental tectosphere, Rev. Geophys. 13 (3) (1975) 1–12.

[104] Y.C. Gung, M. Panning, B. Romanowicz, Global anisotropy and the thickness of continents, Nature 422 (2003) 707–711.

[105] R.K. Kelly, P.B. Kelemen, M. Jull, Buoyancy of the continental upper mantle, Geochem. Geophys. Geosyst. 4 (2) (2003) 1017.

Assist. Prof. MSc. Wenjin Chen, PhD. Dr. Wenjin Chen is the assistant professor in the School of Geomatics Science and Technology at the Nanjing Tech University, Nanjing, China. He received his MSc (2014) and PhD (in 2018) degrees at the Wuhan University. His research interests are mainly related with gravimetric modelling of Earth's inner structure. He is the author of 17 research journal articles (15 records on Scupus/WoS).

Assist. Prof. Ing. Robert Tenzer, PhD, Ph.D. Dr. Tenzer is the assistant professor in the Department of Land Surveying and Geo-Informatics at the Hong Kong Polytechnic University. He received MSc in Geodesy and Cartography (in 1995) and PhD in Physical Geodesy (in 1999) at the Slovak Technical University, as well as PhD in Satellite Geodesy (in 2008) at the Czech Technical University. Between 2001 and 2008, he held research positions at the University of New Brunswick, the University of Newcastle upon Tyne and the Delft University of Technology. Between 2009 and 2012, he taught at the University of Otago. Between 2012 and 2016, he was a visiting professor in the School of Geodesy and Geomatics at the Wuhan University. His research interests cover broad areas of Geodesy, Geophysics, Geodynamic and Planetary Science, with a major focus on geospatial modelling techniques and interpretations, theoretical geodesy and geophysics, geo-referencing, planetary inner structure and processes. He is the author of 4 books and more than 200 research journal articles (155 records on Scupus, 129 records on WoS). He presented his research in 195 conference contributions and 60 invited lectures at universities around the world. He is the member of editorial board and scientific adviser to several journals, while also contributing as the reviewer to more than 40 journals (including Nature Geoscience). Currently, he is the chair of the International Association of Geodesy (IAG) study group IC-SG7: Earth's inner structure from combined geophysical sources.